ADVANCED MATERIALS INTERFACES
www.advmatinterfaces.de

A Halogen-Free and Flame-Retardant Sodium Electrolyte Compatible with Hard Carbon Anodes

*Lars Olow Simon Colbin, Ronnie Mogensen, Alexander Buckel, Yong-Lei Wang, Andrew J. Naylor, Jolla Kullgren, and Reza Younesi**

For sodium-ion batteries, two pressing issues concerning electrolytes are flammability and compatibility with hard carbon anode materials. Non-flammable electrolytes that are sufficiently stable against hard carbon have—to the authors' knowledge—previously only been obtained by either the use of high salt concentrations or additives. Herein, the authors present a simple, fluorine-free, and flame-retardant electrolyte which is compatible with hard carbon: 0.38 M sodium bis(oxalato)borate (NaBOB) in triethyl phosphate (TEP). A variety of techniques are employed to characterize the physical properties of the electrolyte, and to evaluate the electrochemical performance in full-cell sodium-ion batteries. The results reveal that the conductivity is sufficient for battery operation, no significant self-discharge occurs, and a satisfactory passivation is enabled by the electrolyte. In fact, a mean discharge capacity of 107 ± 4 mAh g^{-1} is achieved at the 1005th cycle, using Prussian white cathodes and hard carbon anodes. Hence, the studied electrolyte is a promising candidate for use in sodium-ion batteries.

1. Introduction

The questionable sustainability of the state-of-the-art lithium-ion batteries has sparked an interest in developing rechargeable batteries based on naturally abundant elements, such as a cobalt- and nickel-free sodium-based alternative.[1] However, sodium-ion batteries are unlikely to replace the lithium counterpart in applications requiring high energy densities. Still, sodium-ion batteries may provide a viable alternative for applications where the specific energy density is less important, for example, stationary energy storage. Yet, this is only justified if sodium-ion batteries are superior to lithium-ion batteries in terms of sustainability, cost, and safety. Production needs to be sustainable and the materials must be abundant, cheap, and non-toxic.

Toxicity is however not the only safety concern. Incidents due to the flammability of lithium-ion batteries are frequently reported in media. The flammability of these devices is typically related to the non-aqueous electrolyte. The electrolyte also contributes to the toxicity and high cost, partly due to the use of fluorinated salts.[2–5] Addressing these flaws becomes especially important for sodium-ion batteries, since sustainability and safety is paramount. Fortunately, there is a drive to address the flammable nature of the electrolytes used in batteries. One common tactic to mitigate the flammability is to use organophosphorus compounds as the electrolyte solvent.[6–12] Organophosphorus compounds are a common class of flame retardants used in a variety of applications.[13] However, several of these compounds have a negative impact on the environment and health.[14,15]

For sodium-ion batteries, Liu et.al. formulated an electrolyte which was both non-flammable and used a fluorine-free salt.[10] Their proposed electrolyte based on $NaClO_4$ in trimethyl phosphate (TMP) was an important step towards realizing a non-flammable fluorine-free electrolyte for sodium-ion batteries. However, $NaClO_4$ had to be used at a high concentration (2.5 M), together with 5 vol% fluoroethylene carbonate, to achieve sufficient passivation of the hard carbon electrode. That is, the solid electrolyte interphase (SEI) was inadequate at low salt concentrations and without the use of a fluorinated additive. Moreover, $NaClO_4$ is generally considered to be inappropriate for commercial applications. In connection with non-flammable fluorine-free electrolytes, we recently discovered that sodium bis(oxalato)borate (NaBOB) is soluble in TMP, where the performance of this combination was investigated for battery applications.[16] The SEI was, here too, initially lacking. Yet, the addition of 10 vol% vinylene carbonate enabled a sufficient passivation, resulting in promising battery cycling–without the use of a high salt concentration or fluorine. Despite these advancements, both aforementioned electrolytes share a flaw. TMP has been shown to have adverse effects on organisms[17,18] and currently carries the hazard classification GHS08 (Health hazard) and GHS07 (Harmful). To improve the safety, we attempted to lessen the toxicity by investigating the use of triethyl phosphate (TEP) in a new electrolyte.

TEP has previously been used as the solvent for both lithium- and potassium-based electrolytes.[19,20] TEP currently

L. O. S. Colbin, R. Mogensen, A. Buckel, A. J. Naylor, J. Kullgren, R. Younesi
Department of Chemistry-Ångström Laboratory
Uppsala University
Box 538, Uppsala SE-75121, Sweden
E-mail: reza.younesi@kemi.uu.se
Y.-L. Wang
Department of Materials and Environmental Chemistry
Arrhenius Laboratory
Stockholm University
Stockholm SE-10691, Sweden
The ORCID identification number(s) for the author(s) of this article can be found under https://doi.org/10.1002/admi.202101135.

DOI: 10.1002/admi.202101135

only carries the hazard classification GHS07; it has even been proposed that small amounts of TEP could safely be used as a food additive.[21] However, adverse effects on organisms have been observed when large amounts were consumed[21] or when it was directly injected into embryos.[22] Nevertheless, the combination of TEP and NaBOB produces an electrolyte that is relatively benign, and which consists of cheap and safe components. We employed a variety of electrochemical techniques to evaluate the cycling performance of the electrolyte, in combination with a hard carbon anode and Prussian white cathode in sodium-ion full-cells. The electrolyte showed promise, even when used under harsh cycling conditions. In fact, the performance alone is noteworthy, regardless of the anticipated low cost, apparent non-toxicity, and flame-retardant properties.

2. Results and Discussion

2.1. Physical Properties

Even if TEP is a well-known flame retardant, it was still important to confirm that NaBOB did not unexpectedly inhibit the flame-retardant properties of TEP. The flammability was assessed by exposing a cotton cloth, soaked in a 0.38 M NaBOB-TEP electrolyte, to a butane flame; a dry cotton cloth was used as reference. As expected, the dry cloth burned with vigor until completely charred (**Figure 1**a,b). In contrast, no self-sustaining flame was observed after igniting the soaked cloth (Figure 1c,d). An intensified flame was observed during ignition. Yet, this flame was quenched immediately after the ignition source was removed. Recordings of the flammability experiments are available as Supporting Information.

The characteristic property of an electrolyte is the ability to conduct ions. For battery electrolytes, there is a trend to create formulations with the intent to achieve a high salt concentration.[23] However, electrolytes that can support high currents, while sufficiently passivating the electrodes, despite low salt concentrations, are advantageous. A lower salt concentration would generally reduce electrolyte's cost, viscosity, and degree of ion-pairing. Essentially, a lower concentration should result in more efficient electrolytes. Disregarding efficiency for now, the conductivity must be sufficient for use in batteries. The conductivity was measured over a temperature ranging from −115 to 80 °C (Figure 1e). At room temperature, conductivity of this electrolyte was 5 mS cm^{-1} (Figure 1e inset). It was found that 0.367 mol kg^{-1} NaBOB in TEP exceeded 1 mS cm^{-1} already at −30 °C. For the relation between molar and molal concentrations, see Equation S2, Supporting Information, describing the density as a function of temperature and concentration; for example, 0.367 mol kg^{-1} corresponds to 0.38 M at 20 °C. Furthermore, at 0.37 M (at 20 °C) the viscosity (η) was 2.674 mPas, which is slightly lower than pure propylene carbonate at the same temperature (2.7635 mPas).[24] The temperature dependence of the viscosity and fittings to the Vogel–Fulcher–Tammann equation (Equation S4, Supporting Information) at different concentrations are provided in Figure S2, Supporting Information.

In the interest of conduction efficiency, we also studied the degree of ion-pairing. Even moderate salt concentrations may lead to significant ion-pairing.[25] This would entail that the salt is not being used to its full potential. Furthermore, assuming a consistent equilibrium constant for this process, the pairing would increase with concentration, making the electrolyte less efficient. The percentage of sodium-ions in contact with BOB-anions, was determined using a molecular dynamics (MD) simulation. The simulated model depicted a system corresponding to 0.4 M NaBOB in TEP. Here, the double bonded oxygens on the BOB-anion were predicted to be the predominant coordination sites for the sodium-ion. Sodium-ions were therefore determined to be paired if they were closer than 5.55 Å to a double bonded oxygen on the anion, see **Figure 2**a. The simulation predicted that 35% of the sodium-ions would be paired with a BOB-anion at 0.4 M. This is in line with the measured dissociation constant K_d = 0.31 mol L^{-1} (Figure S4 and Table S3, Supporting Information), which leads to an ion pairing of 42% at 0.4 M. This degree of ion-pairing is similar to that of $LiClO_4$ in γ-Butyrolactone, where an ion-pairing of 41% was reported at 0.467 M;[25] corresponding to 38% paired ions at 0.4 M.

A moderate ion-pairing, at most, was also suggested by IR measurements. Identification of the different vibrations in the spectra was guided by the use of density functional theory (DFT) calculations (see Figure S5, Supporting Information). We deduced that the vibrational band ≈1800 cm^{-1} was mainly caused by the vibrations of the carbon-oxygen double bond of the BOB-anion, highlighted in Figure 2c. The peak at 1807 cm^{-1}

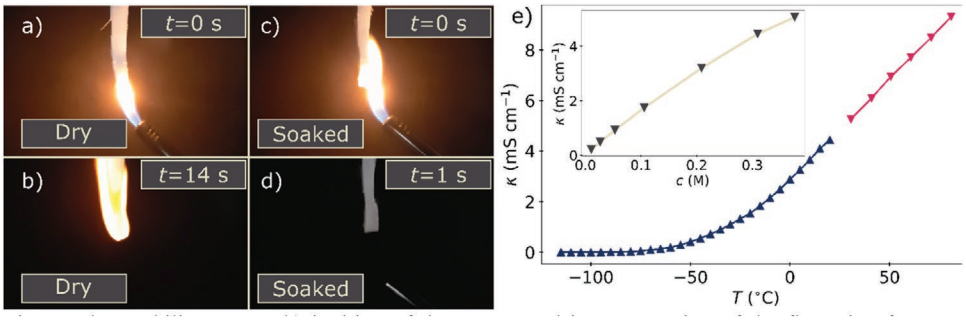

Figure 1. Flammability test: a,b) ignition of dry cotton and its propagation of the flame in after 14 s. c,d) Ignition of cotton soaked in NaBOB-TEP electrolyte and its instant self-extinction of the flame. t is the time after ignition. e) The conductivity of NaBOB in TEP (0.377 mol kg^{-1}) at different temperatures. The two series distinguishes the technique used to achieve the temperature (red means heating on hotplate, and blue means heating by ambience after cooling with liquid nitrogen). The insert depicts the conductivity for different concentrations at room temperature. The values for the concentrations and conductivities are provided as in Table S1, Supporting Information.

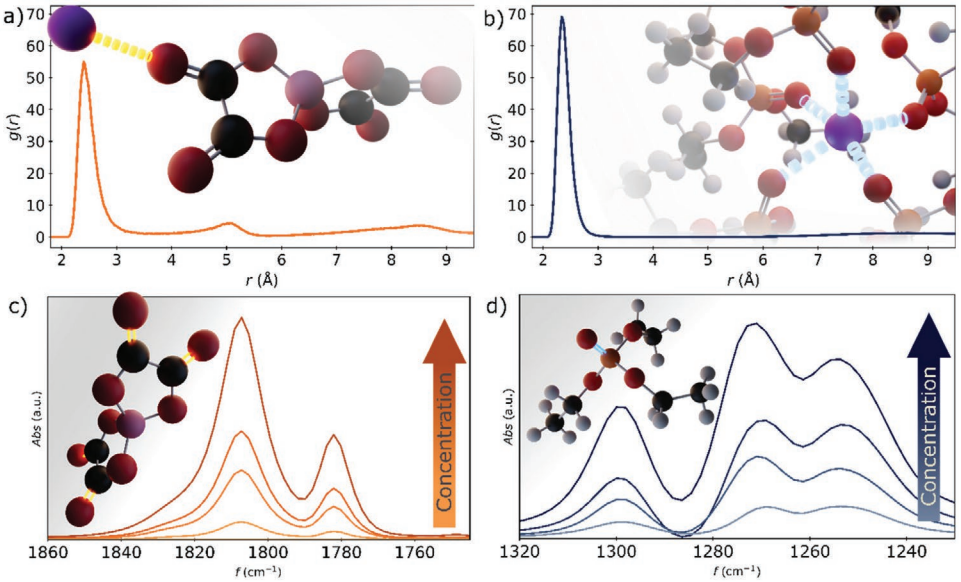

Figure 2. The radial distribution function for a) paired sodium-ions and the BOB-anion's coordinating oxygen; b) free sodium-ions and the double bonded oxygen on TEP. The differential IR absorption with increasing salt concentration, for the double bonded oxygens on c) the BOB-anion and d) the TEP molecule.

was identified to be predominated by a stretch which was symmetrical stretching around the adjacent carbon–carbon bond, and asymmetrical around the screw plane. Conversely, the vibration at 1782 cm^{-1} was an asymmetrical stretch around the carbon–carbon bond, which in turn was symmetrical around the screw plane. When sodium ions are coordinated by the anion, the DFT simulation predicted a shift, and addition of new vibrational modes in this region. We therefore interpret the uniform rise in the differential spectra (Figure 2c) to indicate a relatively low tendency for ion-pairing, that is, a K_d of magnitude 10^{-1} mol L^{-1} or larger.[26]

The simulations and IR measurements also gave information about the fully solvated ions. First, we found no indication from the MD simulation that the BOB-anion adopted a specific coordination structure (Figure S6, Supporting Information). Conversely, the solvent seemed to have a distinct preferred orientation towards the sodium-ions. This was indicated by the radial distribution function, obtained from the free ions (Figure 2b). Here, the double bonded oxygen on the TEP molecule was identified as the coordinating atom, which was attested by the optimized structure using DFT calculations (Figure 2b), and by the IR differential spectra (Figure 2d). The phosphor–oxygen double bond is expected to have two distinct peaks at 1277 and 1262 cm^{-1}.[27] The differential spectra revealed three distinct increases in intensities in this region as the concentration of NaBOB increased, implying the coordination of the double bonded oxygen. Integration of the radial distribution function in Figure 2b gives a value of 4.83; indicating that the fully solvated sodium ions is coordinated by five TEP molecules. Furthermore, both methods (MD and DFT) showed a tendency for a coordination structure with a square pyramidal geometry (Figure 2b).

2.2. Cycling Performance

The electrolyte's performance in batteries was tested by galvanostatic cycling of full-cells, using hard carbon anodes and Prussian white cathodes at three temperatures: 30 °C, 60 °C, and at room temperature. Cycling with metallic sodium as the anode can produce results that are not representative for a feasible system.[28] Hard carbon was therefore chosen as the anode since it is a promising material. However, hard carbon electrodes generally cause poor initial Coulombic efficiencies, which in large part is governed by the electrolyte.[29–31] Yet, the Coulombic efficiencies can also vary significantly for different hard carbon materials,[32] this needs to be kept in mind when comparing results from different studies. When NaBOB in TEP (0.38 M) was used as the electrolyte, the initial Coulombic efficiency was 77% during cycling at room temperature. It is noteworthy that the initial Coulombic efficiency increased with temperature; cycling at 60 °C resulted in an 84% efficiency (Figure 3a). A higher temperature should increase the solubility of SEI compounds, causing an inept SEI formation. Yet, this was evidently not the case. Moreover, a rapid rise in Coulombic efficiency was displayed by all cells (**Figure 3**a), indicating an effective passivation of the hard carbon surface, that is, an effective SEI formation. A higher temperature also appeared to be beneficial even during prolonged cycling. Here the retention from the 6th to 100th cycle increased from 93% to 96% when increasing the temperature from 30 to 60 °C (Figure 3). A comparison of the initial Coulombic efficiency and capacity after 500 cycles, using a variety of electrolytes in a similar system is provided in Table S4, Supporting Information.

Cycling voltammetry measurements were performed to better view the different electrochemical processes. All voltammetry experiments were performed using a Prussian white reference electrode and a Prussian white counter electrode. This was necessary since an immersion test (Figure S7, Supporting Information) revealed that metallic sodium was not stable against the electrolyte–as is common, regarding this feeble metal. Aluminum and carbon coated aluminum foils were used as working electrodes in oxidative cyclic voltammetry scans. Small irreversible currents were observed as the

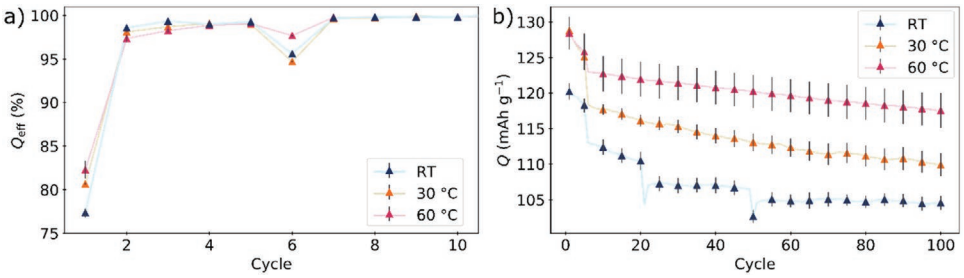

Figure 3. Galvanostatic cycling of a Prussian white cathode against a hard carbon anode, using 0.38 M NaBOB in TEP as the electrolyte. a) Coulombic efficiency Q_{eff} over the first 10 cycles for cycling at 30 °C, 60 °C, and at room temperature; first five cycles at 0.2 C and the following at 1 C. Each cycle is marked with an error bar. b) Average discharge capacity over 100 cycles at 30 °C, 60 °C, and room temperature. The connecting line represents the average discharge capacity for each cycle over three replicates, and every fifth discharge is shown with an error bar depicting the standard deviation. The apparent discontinuity at room temperature is due to pause tests; discussed in a later section.

potential was increased. Yet, in both cases, the current was lessened over each successive sweep (Figures S8 and S9, Supporting Information). This indicates that the electrolyte can sufficiently passivate aluminum; a substantial current would be expected beyond ≈4 V versus Na^+/Na if corrosion of aluminum was occurring.[33] Hard carbon and carbon coated aluminum were respectively used as working electrodes for cyclic voltammetry with a reducing scan direction. Both room temperature and 60 °C measurements were performed using the carbon coated aluminum foil. In all cases, a clear irreversible peak was observed with an onset ≈1.4 V versus Na^+/Na (Figures S10–S12, Supporting Information). This peak is related to the irreversible decomposition of NaBOB.[16] This is also in agreement with what has been observed and discussed for lithium bis(oxalato) borate.[34]

The increased temperature affected the voltammetry response in two distinct ways. At 60 °C the capacity of BOB decomposition peak was greatly reduced, compared to the room temperature measurement (Figures S11–S12, Supporting Information). Yet, additional electrochemical processes took place at an elevated temperature. At least two additional irreversible processes were observed below 1 V versus Na^+/Na that receded over consecutive sweeps. Moreover, a sparse reversible process was also present, with an equilibrium potential at ≈0.07 V versus Na^+/Na. Apart from the faster passivation towards the BOB decomposition, the additional irreversible processes may create a more efficient SEI. This would explain the improved retention at 60 °C (Figure 3b).

As stated previously; the conductivity needs to be sufficient to allow battery cycling. Rate tests were performed to evaluate if the conductivity could allow for cycling at relatively large currents. We found that a current density of 2.7 mA cm^{-2} could be carried by the electrolyte (0.38 M) without a particularly high polarization (**Figure 4**b). The electrolyte's ability to support, at least, moderate current densities, despite a sparse salt concentration is shown by the retention in Figure 4a.

2.3. Surface Analysis

The electrochemical measurements indicated that an efficient SEI formed during the first cycles. Synchrotron-based X-ray photoelectron spectroscopy (XPS) with three different excitation energies was used to study this further. The C 1s spectra of the electrodes cycled to different extents, using a constant current (Figures S10–S17, Supporting Information) are compared to the spectra of pristine and soaked electrodes in **Figure 5**. For the pristine electrode, an asymmetric peak was observed at ≈284.5 eV, highlighted in (i) region, attributed to the sp^2 electrons of the hard carbon material.[35] The peaks at higher binding energies became more prominent when measuring the samples with shallower probing depth (970 and 2350 eV), thus indicating those peaks are originated from SEI. The spectra show only the very surface of the hard carbon electrode was notably affected when the electrodes had been stored under an open circuit voltage (OCV) for 36 h in a full-cell. Interestingly, there was only a slight

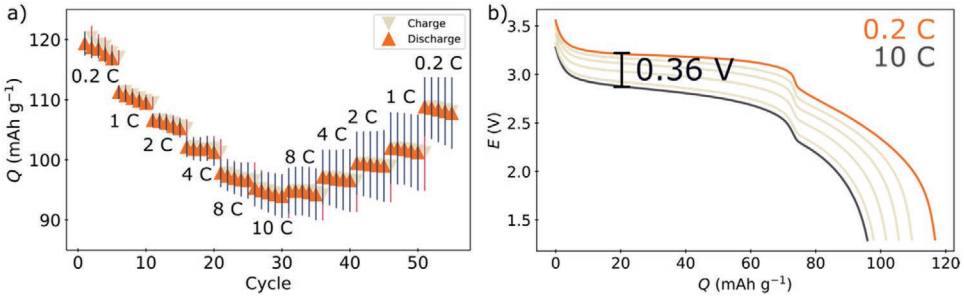

Figure 4. a) Average discharge and charge capacities for the rate-test where each charge and discharge is shown with an error bar (vertical line) signifying the standard deviation. The currents are stated as C-rates. b) The polarization of the voltage profile for a discharge at different C-rates. The difference in overpotential (at 20 mAh g^{-1}) between 0.2 and 10 C is highlighted in the figure.

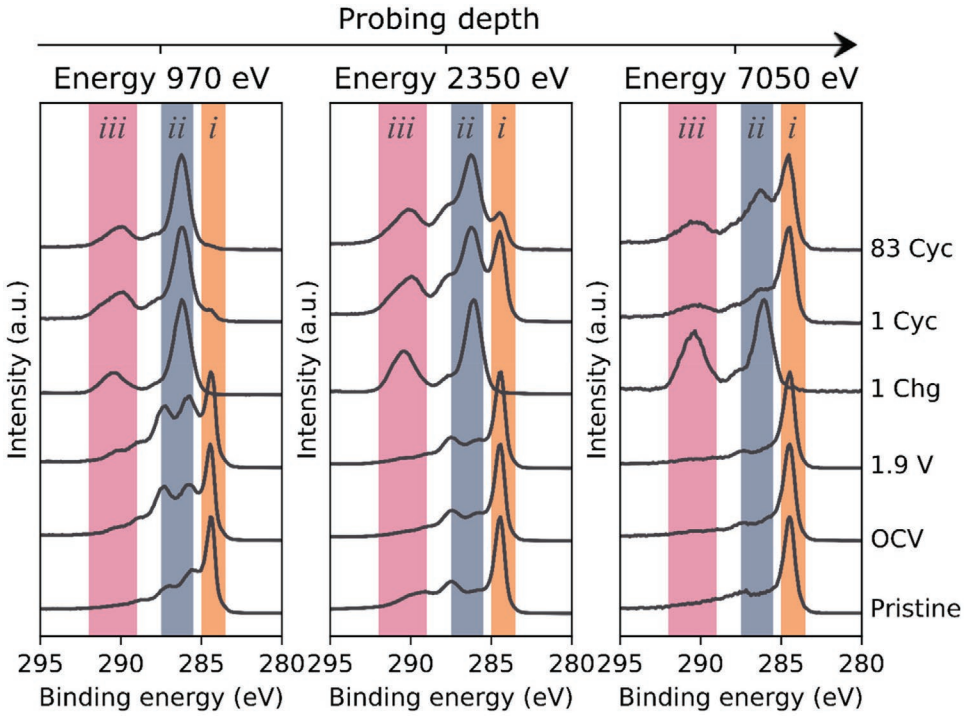

Figure 5. The C1s spectra of hard carbon electrodes: pristine, 36 h on OCV, charged to 1.9 V in a full cell (Figure S13, Supporting Information), 1 Chg (Figure S14, Supporting Information), 1 Cyc (Figure S15, Supporting Information), and 83 Cyc (Figures S16 and S17, Supporting Information). Each electrode was measured with the photon energies 970, 2350, and 7050 eV. The regions marked with i, ii, and iii highlight peaks used to distinguish the hard carbon substrate (i), from the SEI (ii and iii).

difference between the electrode stored under OCV and the one that had been charged to 1.9 V. This is despite that the charging to 1.9 V over an extra plateau is equivalent to 16 mAh g^{-1}, amounting to 10% of the capacity for the first charge (Figures S13 and S14, Supporting Information). Though this plateau is likely connected to the decomposition of the BOB-anion, it is noteworthy that it did not leave a detectable solid species on the surface of the electrode. However, all samples were washed with pure TEP solvent before the XPS measurement. It is therefore possible that any passivating layer formed at this stage might have been dissolved during sample preparation.

At all excitation energies, the fully charged electrode displayed none of the features of the substrate. Here, two distinct peaks appeared; one at ≈286 eV, the other at 290 eV (region [i] and [ii] in Figure 5). These completely replaced all signals from the substrate, indicating the formation of thick SEI blocking probing the hard carbon substrate. This means that the thickness of the SEI was at least 40–50 nm. However, once a full cycle had been completed, the substrate was again partly visible implying that the SEI became thinner. A clear gradient was here seen with increasing probing depth. The peaks that appeared, after the charge, remained the most prominent feature at the outer surface region. The electrodes after 1 and 83 cycles display similar features in the XPS spectra indicating that the SEI becomes quite stable after 1 cycle.

2.4. Pause Test

The electrolyte seemed to enable quite stable cycling, at least for the first 100 cycles (Figure 3). However, there is always a risk that detrimental electrolyte-fuelled side reactions are taking place. The effect of these reactions could be suppressed until later cycles, or slowly but surely consume the capacity of the battery. It is therefore important to identify the extent of unwanted side reactions occurring within the cell.

The amount and characteristics of side reactions were investigated using pause tests.[36,37] Here, the manifestation of self-discharge during open-circuit conditions is typically an indication of antagonistic reactions within the cell. The electrolyte would typically be partly responsible for a self-discharge by poor surface passivation and formation of readily oxidizable compounds which results in redox shuttling. As a matter of fact, in sodium-ion batteries, hard carbon has been shown to be especially prone to self-discharge.[38]

The pauses were performed by holding the cell at open-circuit conditions for 100 h: once in a discharged state and twice in a charged state, as shown in **Figure 6**. A change in potential during the pause would indicate a self-discharge, and thus unwanted processes. During the pause after discharge, the potential shifted by 38 ± 2 mV (0.39 mV h^{-1}), excluding an initial 3-h relaxation (Figure 6b). By the same criteria, pauses at a charged state after the 21st and 50th charge resulted in a potential shift of 113 ± 4 (1.16 mV h^{-1}) and 98 ± 3 mV (1.00 mV h^{-1}), respectively (Figure 6c,d). During both pauses after a charge, the OCV never descended upon the upper plateau of the Prussian white cathode. The upper plateau has a working potential at 3.3 V versus Na^+/Na, corresponding to ≈3.24 V in a full-cell. A moderate self-discharge would result in an OCV at this potential–or an even lower potential for a severe self-discharge. The OCV was higher than 3.3 V, which indicates that redox shuttling was minimal. It is likely

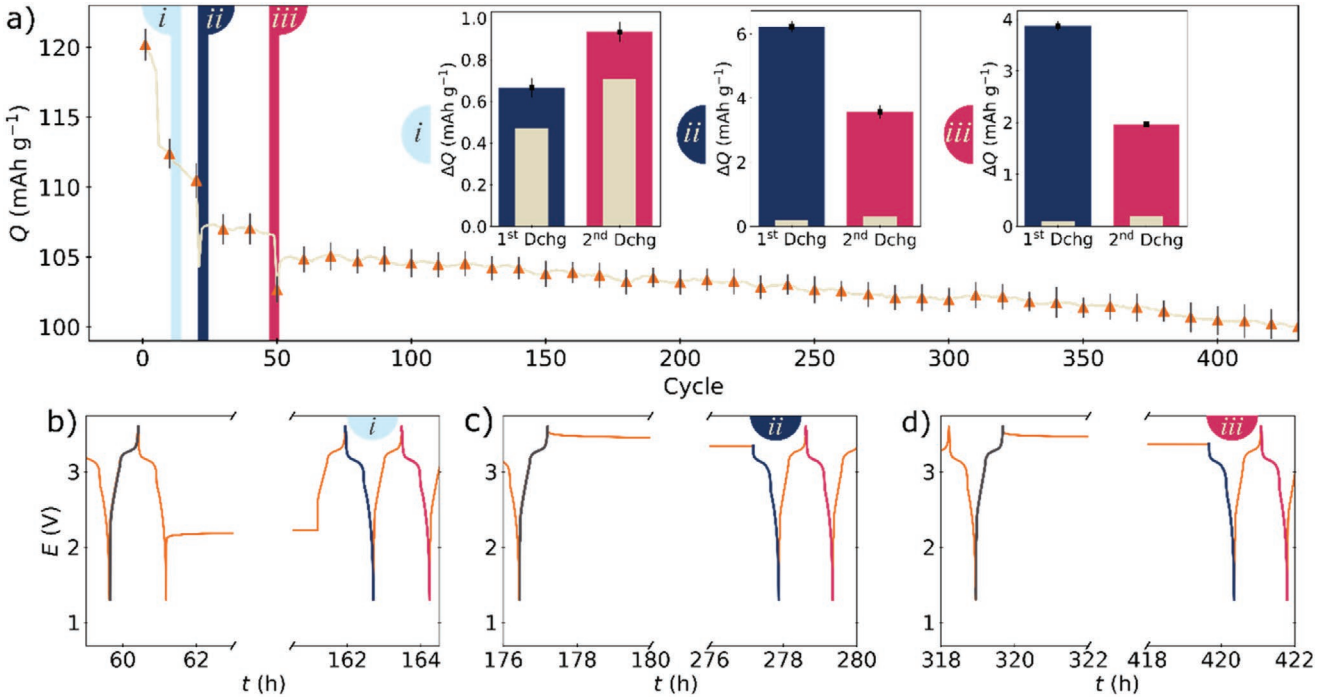

Figure 6. a) The discharge capacity for a cell subjected to pause testing. The pauses were performed by holding the cell at open circuit conditions for 100 h at cycle 10, 21, and 50. The capacity losses during each pause are shown in inset i, ii, and iii in (a), which correspond to the first (b), second (c), and third pause (d), respectively. These inserts are the differences between the capacity of the last charge before the pause, and the first or second discharge after the pause. The Dutch White bars represent an expected decrease in capacity, based on the Coulombic efficiency of the last cycle before the pause.

that relaxation of concentration gradients contributed to the observed shift.

The capacity losses observed during the pauses can be used to distinguish between different capacity draining processes. The pauses can also be used to evaluate whether these processes permanently impede the capacity, or if the capacity can be recovered. This is done by comparing the two subsequent discharges after the pause with the charge prior pause, illustrated by the coloring in Figure 6. Moreover, to perceive finer details, it is necessary to compare these losses with the general Coulombic efficiency. Here, the recorded efficiency for the cycle before the pauses was used to extrapolate an "expected" loss due to normal cycling, see Dutch White bars in insets (i), (ii), and (iii) in Figure 6a. From this, one can conclude that all capacity lost during the first pause (discharged state) was permanent, albeit small (0.002 mAh g^{-1} h^{-1}). In contrast, a discrepancy was observed between the loss for the first and second discharge during pauses at a charged state. Here, approximately half the capacity loss during the pause was recoverable. Nevertheless, more capacity was still lost permanently during pauses at a charged state. Yet, the overall loss was lower during the pause at cycle 50 than at cycle 21.

The recoverable loss is likely not an issue for the longevity of the batteries. Especially since it was lessened at a higher cycling index. The rate of the recoverable capacity loss was 0.028 and 0.020 mAh g^{-1} h^{-1} for the pauses after 21 and 50 cycles, respectively. This corresponds to 0.025% h^{-1} and 0.019% h^{-1} of the capacity for the cycle prior pause. Moreover, the recoverable capacity loss is likely coupled with the shift in voltage during the pause, and thus caused by the similar processes. This is indicated by the coinciding trend in magnitude of voltage shift for the pause at a higher cycling index.

Permanent losses are however a more pressing concern. The difference between the rates of permanently lost capacity during the different pauses gives clues about the processes taking place. At a discharged state it is unlikely that wide variety of parasitic processes would occur. However, one possible reason for a permanent capacity loss would be the dissolution of the SEI. A capacity loss due to dissolution would occur if there is even a minimal solubility of the SEI species in the electrolyte solvent.[39] In contrast, at a charged state, additional processes become more plausible as causes for the permanently lost capacity. In particular, three debated processes would reflect on the trend that the permanent loss is lower at a higher cycling index. The first being electron diffusion through the SEI,[40] the second would be solvent diffusion through the SEI,[41] and the third would be saturation of the electrolyte by SEI species.[39] The rate for either of these processes would decrease as they progress. That is, any of these mechanisms could explain the lower permanent loss during a charged pause at a higher cycling index; 0.018 mAh g^{-1} h^{-1}, compared to 0.032 mAh g^{-1} h^{-1}.

The retention during cycling should be coupled to the permanent losses observed during the pause tests. Since these scaled with the state of charge, it is possible that the rate of loss would at least be between 0.002 and 0.018 mAh g^{-1} h^{-1}, during the continued cycling. This translates to a permanent loss of 0.56–5.08 mAh g^{-1} from the 100th to 300th cycle. During the actual measurement, a loss of 2.63 ± 0.17 mAh g^{-1} was observed during these cycles. The predicted permanent losses were therefore considered representative for the continued cycling.

However, the width of the predicted span is problematic, since this would correspond to a loss between 4 and 34 mAh g^{-1} for 1000 cycles at 1 C–not accurate enough to give useful insights. Yet, it would be expected that an actual permanent loss would be in the lower end of this range; accounting for decreasing losses at charge states as cycling progresses.

2.5. Resistance

Capacity draining side reactions is not the only cause for cell failure. An increased resistance could also cause an apparent capacity loss since the resistance would cause an overpotential for the desired electrochemical processes, placing them outside an accessible potential range. Such an increase could be caused by a deterioration or complete depletion of the electrolyte, or by formation of resistive surface layers on the surface of the anode or the cathode. This would lead to a fading capacity and, eventually, cell failure. The resistance during cycling was investigated using intermittent current interruption[42] (ICI) performed in a three-electrode setup. This allowed for separate monitoring of the resistance contribution from the cathode and anode (see **Figure 7**).

The results indicate that the anode (Figure 7e) was the main contributor to the cell resistance. In comparison, the cathode only displayed moderate resistances (Figure 7f). Both electrodes exhibited a resistance dependence on the state of charge. This was studied by partitioning the resistance for each electrode into two domains, P1 and P2 (Figure 7b,c). P1 was the first half of the measured resistances of a discharge, whereas P2 was the second half. This partition revealed a continuous increase in resistance on the lower plateau of the Prussian white cathode (Figure 7f). This plateau appears due to the redox of the high spin iron in Prussian white. The higher resistance during the redox of the high spin iron has been observed in a similar system;[43] however, a gradual increase in the resistance was not reported.

The fact that the measured resistance was dependent on the charge state indicates that it is unlikely that the increasing resistance was caused by the electrolyte. Essentially, a resistance increase solely due to a general electrolyte degradation would be independent of the state of charge.

2.6. Long Term Cycling

The predicted retention based on the pause tests and the increasing resistance on the cathode, merited further evaluation of the system's long-term performance. Long-term cycling at 30 °C, 60 °C, and at room temperature is shown in **Figure 8**. As anticipated by the increasing resistance (Figure 7f), all cells reached a critical point after long-term cycling where the capacity was rapidly decreased (Figure 8). The observed polarization (Figure 8b,c) was consistent with the results from the resistance measurements, where the resistance–observed as polarization–was dependent on the state of charge. Furthermore, a comparison of the development of the resistances in Figure 7e,f, suggests that the Prussian white is likely causing the polarization in Figure 8b,c. This in turn implies that the decreasing rate capability was not due to an adverse interaction between hard carbon and the electrolyte.

It would in general be possible that the capacity was simply lost due to accelerated side reactions. In this scenario it would be impossible to regain the lost capacity. However, as the current was lowered, the lower plateau reappeared in the voltage profile and the capacity of the cells seemingly increased (Figure 8c). It is

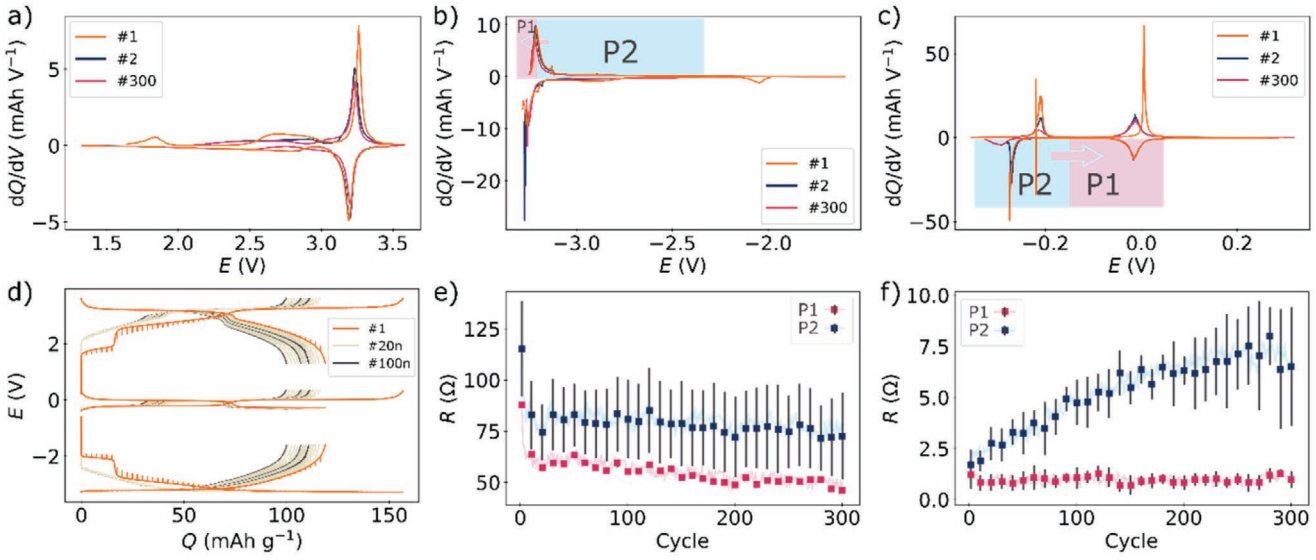

Figure 7. The derivative of the capacity curves for a full-cell (a) with the response from the anode (b) and cathode (c) plotted separately. The boxed regions indicate the partitioned domain underlying the representation of the resistance. The arrow indicates the shift of the regimes due to capacity fading. The potential of the anode and cathode are plotted versus the Prussian white reference electrode, 3.3 V versus Na^+/Na. d) The voltage profile of a three-electrode cell. The median discharge resistance on the anode (e) and cathode (f). Resistances were partitioned by number of data points, where P1 and P2 are the first and second half of the measured resistances for each discharge. The error bars in (e) and (f) represent the median absolute deviation. A more detailed view of each replicate is shown in Figures S18–S20, Supporting Information.

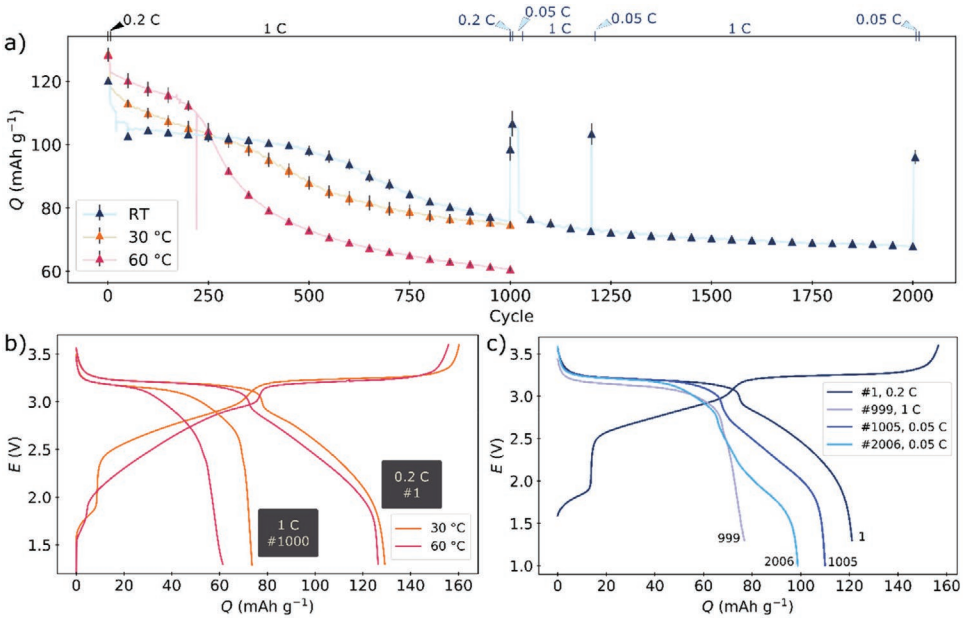

Figure 8. Galvanostatic cycling of a Prussian white cathode against a hard carbon anode, using 0.38 M NaBOB in TEP as the electrolyte. a) Average discharge capacity at 30 °C, 60 °C, and room temperature. Every 50th cycle (and cycle 1, 1005, 2002, and 2006) is marked with an error bar depicting the standard deviation, whereas each cycle is indicated by a connecting line. The notation at the top of the graph shows which C-rate was used in specific regions, note that the 1000th cycle at 30 and 60 °C was done at 1 C. b) Voltage profile of the 1st cycle (0.2 C) and 1000th discharge (1 C) at 30 and 60 °C. c) The voltage profile of the 1st cycle (0.2 C), 999th discharge (1 C), 1005th discharge (0.05 C), and 2006th discharge (0.05 C) at room temperature.

therefore clear that the sudden drop in capacity was not caused by an accelerated permanent loss of active sodium, but rather a decrease in rate capability. In fact, only 10.6 ± 2.0 mAh g^{-1} was lost between the 1005th and 2006th cycle, which agrees with the prediction from the pause tests. This, in combination with the resistance measurements, implies that the electrolyte was not causing the sharp decrease in capacity (Figure 8). In this regard, the electrolyte was outperforming the other components within the system. In fact, in the context of active sodium, 96 mAh g^{-1} remained after 2006 cycles.

3. Conclusion

A flame-retardant, halogen-free electrolyte for sodium-ion batteries was formulated using NaBOB as the salt and TEP as the solvent. The electrolyte enabled good long-term cycling, low self-discharge, and promising rate-performance. In fact, it is likely that the electrolyte had a greater stability than other components within the cell, even without the use of fluorinated compounds or additives. A large part of the observed capacity fading at room temperature was determined to be caused by a decreasing rate capability of the electrodes, rather than the electrolyte. Here, we also showed that pause testing can be used to predict the irreversible capacity loss due to the side reactions involving the electrolyte. Finally, we conclude that the cycling performance, in combination with the flame-retardant properties and apparent non-toxicity of NaBOB and TEP allow for a sustainable alternative to conventional electrolytes. Promising performance, low-cost, and simplicity: NaBOB in TEP is a strong candidate as an electrolyte for use in sodium-ion batteries with hard carbon anodes.

4. Experimental Section

NaBOB was synthesized according to the procedure reported by Whittingham et al.,[44] with the added purification step reported by Mogensen et al.[16] TEP ≥99.8% was produced by Acros and bought through Merck. Prior to use, the solvent was dried with activated molecular sieves, resulting in a water content of 12 ppm, according to Karl Fischer titration.

The electrolytes were prepared solely relying on the masses of the components, resulting in concentrations in units of molal. The molar concentrations were then calculated using the density (Equation S2, Supporting Information).

Cotton cloths were used as substrate in the flammability tests. Here a dry cloth and a cloth soaked in the NaBOB in TEP electrolyte was exposed to a butane flame. Each attempt was video recorded and evaluated based on self-extinction of the flame. The time of self-extinction was extracted from the runtime of the recording.

Conductivity measurements, shown in the main article, were performed using a Mettler Toledo SevenGo Duo pro pH/ORP/Ion/Conductivity meter SG78 with an InLab 738ISM probe. The conductivity measurements were carried out in a glove box (O_2 < 1 ppm, H_2O < 1 ppm) when recorded at room temperature and elevated temperatures. The measurement on the cooled electrolyte was done under ambient conditions; liquid nitrogen was used to cool the electrolyte together with an aluminum block acting as a heat buffer. The conductivity was continually recorded as ambiance slowly warmed the electrolyte. Care was taken to prevent condensed water and ice from perturbing the measurement. With this in mind, a final conductivity was recorded once the electrolyte had been heated to room temperature.

Galvanostatic cycling was performed in pouch cells. All of these experiments were performed with three replicates. Data depicting

replicates are presented as mean values along with the associated standard deviation. Cycling was typically set to use the cut-off potential 1.3 and 3.6 V; however, the lower limit was reduced to 1 V after 1000 cycles. Cycling at 30 and 60 °C was performed at 1 C (148 mA g^{-1} Prussian white, 132 mA g^{-1} hard carbon) after 5 initial cycles at 0.2 C (29.7 mA g^{-1} Prussian white, 26.5 mA g^{-1} hard carbon). The 30 °C cycling was performed on a Novonix High Precision Charger System while the 60 °C cycling was facilitated by an Arbin Instruments battery testing system. The pause test cells were cycled at the same rates. However, these cells were held at OCV for 100 h after the 11th discharge, after the 21st charge, and after the 50th charge; which was done on a LANHE CT2001A galvanostat. The ICI-cycling was done at 0.2 C, using ≈1 cm^2 reference electrodes comprised of preconditioned Prussian white. The potential limits were controlled by the full cell potential, even when a dedicated reference was used. The reference therefore only acted as a probe. This enabled individual monitoring of each electrode, while minimizing the possibility of the reference influencing the cycling. Furthermore, a significant change in potential of the reference would be detected by a unison shift in potential for both the anode and cathode. Fortunately, no such shift occurred during the 300 cycles. In the ICI-cycling, the current was interrupted for 1 s every 5 min. To better capture the rate capability of the electrolyte, rate tests were performed by increasing the C-rate of the discharge from 0.2 C (54.4 µA cm^{-2}) up to 10 C (2.73 mA cm^{-2}) followed by a symmetric decrease to 0.2 C, while the C-rate of the charge was held constant at 0.2 C. All C-rates are based on the practical specific capacity of Prussian white, 150 mAh g^{-1}.

DFT was used to parameterize the MD simulations. Here, the Gaussian 16 package (version C.01)[45] was used to calculations at the B3LYP/6-311+G(d,p) level of theory. The Grimme's-D3 dispersion correction with the Becke–Johnson damping (GD3BJ)[46] were used in the calculations to obtain the optimized molecular geometry for the TEP molecule and its intermolecular coordination with sodium-and BOB-ions. The optimized molecular geometries of these molecules are provided in Figures S21 and S22, Supporting Information.

The atomistic force field parameters for TEP were based on the AMBER framework; developed with a similar procedure as described in previous work.[47] The CHELPG atomic partial charges on these molecules were calculated at the same level of theory with the B3LYP hybrid functional and the 6–311+G(d,p) basis set. The cross-interaction parameters between different atom types were obtained from the Lorentz-Berthelot combination rules.

Atomistic MD simulations were performed using the GROMACS package[48] with 3D periodic boundary conditions. The equations of motion were integrated using a leapfrog integration algorithm, with a time step of 1.0 fs. A cut-off radius of 1.6 nm was set for short-range van der Waals interactions and real-space electrostatic interactions. The particle-mesh Ewald summation method with an interpolation order of 5 and Fourier grid spacing of 0.12 nm was employed to handle long-range electrostatic interactions in reciprocal space. All simulation systems were first energetically minimized using a steepest descent algorithm and annealed gradually from 600 to 300 K within 10 ns. Thereafter equilibrated for 40 ns, maintained using the Nose–Hoover thermostat and the Parrinello–Rahman barostat with time coupling constants of 500 and 200 fs, respectively. This was to maintain a temperature at 300 K and pressure at 1 atm. Canonical ensemble (NVT) simulations were further performed for 100 ns for the main simulation, where the trajectories were recorded at an interval of 100 fs for structure and dynamics analysis.

Infrared spectroscopy was measured on a VERTEX 80V/70V system, manufactured by Brucker. The transmission spectra were obtained using an omni cell with CaF_2 windows. The windows had to be spaced solely by a thin film of solvent, due to an overall high absorbance of the solvent. Normalization was therefore performed to account for the difference in path length. The normalization was based on the vibration bands of the C—H ≈2950 cm^{-1}. The backgrounds were also adjusted using a spline function. We believe that this calibration of the spectra does not misconstrue a qualitative interpretation. However, a more elegant method is needed for a quantitative analysis of the intensities.

Supporting Information

Supporting Information is available from the Wiley Online Library or from the author.

Acknowledgements

The authors acknowledge Diamond Light Source for time on Beamline/Lab I09 Surface and Interface Structural Analysis, under Proposal SI26551–1. The research leading to the synchrotron results has been supported by the project CALIPSOplus under Grant Agreement 730872 from EU Framework Programme for Research and Innovation HORIZON 2020. The authors would like to acknowledge the financial support from the Swedish Research Council for Environment, Agricultural Sciences and Spatial Planning (Formas) via the grant 2016-01257, from ÅForsk foundation (ref no. 20–675). The Batteries Sweden (BASE) supported by VINNOVA, and from STandUP for Energy. The computations and data handling were enabled by resources provided by the Swedish National Infrastructure for Computing (SNIC) at Tetralith-NSC, partially funded by the Swedish Research Council through grant agreement no. 2018–05973.

Conflict of Interest

The Prussian white powder used as positive electrode material in this study is a commercial product provided by ALTRIS AB, a company co-founded by R.M. and R.Y. The other authors in this paper declare no conflict of interest.

Author Contributions

L.O.S.C., R.M., J.K, and R.Y. outlined the idea. A.B. and L.O.S.C. prepared the electrolytes and did the conductivity measurements. A.B. conducted the solubility tests and flammability tests. L.O.S.C. performed the electrochemical measurements and cell-assembly. A.J.N. performed the X-ray photoelectron spectroscopy measurement. L.O.S.C. and A.J.N. analyzed the X-ray photoelectron spectroscopy results. L.O.S.C., R.M, and A.B. synthesized NaBOB. Y.-L.W. performed the DFT calculations for the initial parameterization of force field parameters for the BOB-anion and TEP, and thereafter atomistic molecular dynamics simulations of NaBOB-TEP mixtures. L.O.S.C. and Y.-L.W. analyzed the molecular dynamics data. L.O.S.C. performed the viscosity, density, and IR measurements. L.O.S.C. also performed the DFT simulation used for the interpretation of the IR spectra.

Data Availability Statement

All research data related to this work are included in the manuscript and the provided supporting information files.

Keywords

NaBOB, non-flammable electrolytes, organophosphate, sodium bis(oxalato)borate, sodium-ion batteries, triethyl phosphate (TEP)

Received: August 16, 2021
Published online: October 22, 2021

[1] V. Palomares, P. Serras, I. Villaluenga, K. B. Hueso, J. Carretero-González, T. Rojo, *Energy Environ. Sci.* **2012**, *5*, 5884.
[2] M. M. Archuleta, *J. Power Sources* **1995**, *54*, 138.

[3] G. G. Eshetu, J.-P. Bertrand, A. Lecocq, S. Grugeon, S. Laruelle, M. Armand, G. Marlair, *J. Power Sources* **2014**, *269*, 804.
[4] R. Dmello, J. D. Milshtein, F. R. Brushett, K. C. Smith, *J. Power Sources* **2016**, *330*, 261.
[5] R. Younesi, G. M. Veith, P. Johansson, K. Edström, T. Vegge, *Energy Environ. Sci.* **2015**, *8*, 1905.
[6] X. Wang, E. Yasukawa, S. Kasuya, *J. Electrochem. Soc.* **2001**, *148*, A1058.
[7] J. Wang, Y. Yamada, K. Sodeyama, E. Watanabe, K. Takada, Y. Tateyama, A. Yamada, *Nat. Energy* **2018**, *3*, 22.
[8] N. D. Nam, I. J. Park, J. G. Kim, *Met. Mater. Int.* **2012**, *18*, 189.
[9] B. S. Lalia, N. Yoshimoto, M. Egashira, M. Morita, *J. Power Sources* **2010**, *195*, 7426.
[10] X. Liu, X. Jiang, Z. Zeng, X. Ai, H. Yang, F. Zhong, Y. Xia, Y. Cao, *ACS Appl. Mater. Interfaces* **2018**, *10*, 38141.
[11] L. Jiang, C. Liang, H. Li, Q. Wang, J. Sun, *ACS Appl. Energy Mater.* **2020**, *3*, 1719.
[12] H. Yang, Q. Li, C. Guo, A. Naveed, J. Yang, Y. Nuli, J. Wang, *Chem. Commun.* **2018**, *54*, 4132.
[13] A. Granzow, *Acc. Chem. Res.* **1978**, *11*, 177.
[14] G.-L. Wei, D.-Q. Li, M.-N. Zhuo, Y.-S. Liao, Z.-Y. Xie, T.-L. Guo, J.-J. Li, S.-Y. Zhang, Z.-Q. Liang, *Environ. Pollut.* **2015**, *196*, 29.
[15] M. Aboudonia, *J. Environ. Health Sci.* **2016**, *2*, 1.
[16] R. Mogensen, S. Colbin, A. S. Menon, E. Björklund, R. Younesi, *ACS Appl. Energy Mater.* **2020**, *3*, 4974.
[17] E. Bomhard, *Fundam. Appl. Toxicol.* **1997**, *40*, 75.
[18] S. S. Epstein, W. Bass, E. Arnold, Y. Bishop, *Science* **1970**, *168*, 584.
[19] Z. Zeng, V. Murugesan, K. S. Han, X. Jiang, Y. Cao, L. Xiao, X. Ai, H. Yang, J.-G. Zhang, M. L. Sushko, J. Liu, *Nat. Energy* **2018**, *3*, 674.
[20] S. Liu, J. Mao, Q. Zhang, Z. Wang, W. K. Pang, L. Zhang, A. Du, V. Sencadas, W. Zhang, Z. Guo, *Angew. Chem., Int. Ed.* **2020**, *59*, 3638.
[21] M. R. Gumbmann, W. E. Gagné, S. N. Williams, *Toxicol. Appl. Pharmacol.* **1968**, *12*, 360.
[22] C. Egloff, D. Crump, E. Porter, K. L. Williams, R. J. Letcher, L. T. Gauthier, S. W. Kennedy, *Toxicol. Appl. Pharmacol.* **2014**, *279*, 303.
[23] Y. Yamada, J. Wang, S. Ko, E. Watanabe, A. Yamada, *Nat. Energy* **2019**, *4*, 269.
[24] G. Moumouzias, G. Ritzoulis, *J. Chem. Eng. Data* **1992**, *37*, 482.
[25] M. Caillon-Caravanier, G. Bosser, B. Claude-Montigny, D. Lemordant, *J. Electrochem. Soc.* **2002**, *149*, E340.
[26] Y. Marcus, G. Hefter, *Chem. Rev.* **2006**, *106*, 4585.
[27] R. Nyquist, *Interpret. Infrared, Raman, Nucl. Magn. Reson. Spectra* **2001**, *2*, 231.
[28] R. Mogensen, S. Colbin, R. Younesi, *Batteries Supercaps* **2021**, *4*, 791.
[29] D. A. Stevens, J. R. Dahn, *J. Electrochem. Soc.* **2000**, *147*, 1271.
[30] A. Ponrouch, A. R. Goñi, M. R. Palacín, *Electrochem. Commun.* **2013**, *27*, 85.
[31] K.-L. Hong, L. Qie, R. Zeng, Z.-Q. Yi, W. Zhang, D. Wang, W. Yin, C. Wu, Q.-J. Fan, W.-X. Zhang, Y.-H. Huang, *J. Mater. Chem. A* **2014**, *2*, 12733.
[32] L.-F. Zhao, Z. Hu, W.-H. Lai, Y. Tao, J. Peng, Z.-C. Miao, Y.-X. Wang, S.-L. Chou, H.-K. Liu, S.-X. Dou, *Adv. Energy Mater.* **2021**, *11*, 2002704.
[33] K. Matsumoto, K. Inoue, K. Nakahara, R. Yuge, T. Noguchi, K. Utsugi, *J. Power Sources* **2013**, *231*, 234.
[34] K. Xu, S. S. Zhang, U. Lee, J. L. Allen, T. R. Jow, *J. Power Sources* **2005**, *146*, 79.
[35] M. Carboni, J. Manzi, A. R. Armstrong, J. Billaud, S. Brutti, R. Younesi, *ChemElectroChem* **2019**, *6*, 1745.
[36] G. Yan, K. Reeves, D. Foix, Z. Li, C. Cometto, S. Mariyappan, M. Salanne, J. Tarascon, *Adv. Energy Mater.* **2019**, *9*, 1901431.
[37] R. Mogensen, A. Buckel, S. Colbin, R. Younesi, *Chem. Mater.* **2021**, *33*, 1130.
[38] R. Mogensen, D. Brandell, R. Younesi, *ACS Energy Lett.* **2016**, *1*, 1173.
[39] L. A. Ma, A. J. Naylor, L. Nyholm, R. Younesi, *Angew. Chem., Int. Ed.* **2021**, *60*, 4855.
[40] S. Das, P. M. Attia, W. C. Chueh, M. Z. Bazant, *J. Electrochem. Soc.* **2019**, *166*, E107.
[41] H. J. Ploehn, P. Ramadass, R. E. White, *J. Electrochem. Soc.* **2004**, *151*, A456.
[42] M. J. Lacey, *ChemElectroChem* **2017**, *4*, 1997.
[43] L. Wang, J. Song, R. Qiao, L. A. Wray, M. A. Hossain, Y.-D. Chuang, W. Yang, Y. Lu, D. Evans, J.-J. Lee, S. Vail, X. Zhao, M. Nishijima, S. Kakimoto, J. B. Goodenough, *J. Am. Chem. Soc.* **2015**, *137*, 2548.
[44] P. Y. Zavalij, S. Yang, M. S. Whittingham, *Acta Crystallogr., Sect. B: Struct. Sci.* **2003**, *59*, 753.
[45] Gaussian 09, Revision A.02, M. J. Frisch, G. W. Trucks, H. B. Schlegel, G. E. Scuseria, M. A. Robb, J. R. Cheeseman, G. Scalmani, V. Barone, G. A. Petersson, H. Nakatsuji, X. Li, M. Caricato, A. Marenich, J. Bloino, B. G. Janesko, R. Gomperts, B. Mennucci, H. P. Hratchian, J. V. Ortiz, A. F. Izmaylov, J. L. Sonnenberg, D. Williams-Young, F. Ding, F. Lipparini, F. Egidi, J. Goings, B. Peng, A. Petrone, T. Henderson, D. Ranasinghe, V. G. Zakrzewski, J. Gao, N. Rega, G. Zheng, W. Liang, M. Hada, M. Ehara, K. Toyota, R. Fukuda, J. Hasegawa, M. Ishida, T. Nakajima, Y. Honda, O. Kitao, H. Nakai, T. Vreven, K. Throssell, J. A. Montgomery Jr., J. E. Peralta, F. Ogliaro, M. Bearpark, J. J. Heyd, E. Brothers, K. N. Kudin, V. N. Staroverov, T. Keith, R. Kobayashi, J. Normand, K. Raghavachari, A. Rendell, J. C. Burant, S. S. Iyengar, J. Tomasi, M. Cossi, J. M. Millam, M. Klene, C. Adamo, R. Cammi, J. W. Ochterski, R. L. Martin, K. Morokuma, O. Farkas, J. B. Foresman, D. J. Fox, Gaussian, Inc., Wallingford CT **2016**.
[46] S. Grimme, J. Antony, S. Ehrlich, H. Krieg, *J. Chem. Phys.* **2010**, *132*, 154104.
[47] Y.-L. Wang, F. U. Shah, S. Glavatskih, O. N. Antzutkin, A. Laaksonen, *J. Phys. Chem. B* **2014**, *118*, 8711.
[48] M. J. Abraham, T. Murtola, R. Schulz, S. Páll, J. C. Smith, B. Hess, E. Lindahl, *SoftwareX* **2015**, *1–2*, 19.